Growth, characterizations, and thermal analysis of rhenium chalcogenides ReS$_{2-x}$Se$_x$ (*x* = 0, 1, and 2) single crystals

Atriy Ghetiya[1,*] ⓘ, Sunil H. Chaki[1,2,*], Jiten P. Tailor[3], and M. P. Deshpande[1]

[1] P. G. Department of Physics, Sardar Patel University, Vallabh Vidyanagar, Anand, Gujarat 388120, India
[2] Department of Applied and Interdisciplinary Sciences, Sardar Patel University, Vallabh Vidyanagar, Anand, Gujarat 388120, India
[3] Physics Department, M. B. Patel Science College, Anand, Gujarat 388001, India

ABSTRACT

The rhenium chalcogenides ReS$_{2-x}$Se$_x$ (*x* = 0, 1, and 2) single crystals are grown at low temperature from the melting point by chemical vapor transport technique. The powder X-ray diffraction analysis of the single-crystals symmetry showed orientation at (001) plane of ReS$_{2-x}$Se$_x$ (*x* = 0, 1, and 2). The energy-dispersive analysis of X-rays showed the crystals to be pure. The optical bandgap obtained of the as-grown single crystals falls in visible range of 1.27 eV to 1.37 eV. The Raman peaks are well assigned to both in-plane and out-of-plane vibrations in the ReS$_{2-x}$Se$_x$ (*x* = 0, 1, and 2). The thermal gravimetric analysis showed that given as-grown single crystals are stable up to nearly 650 K and the differential thermal gravimetric analysis showed that single crystals disintegrate in two steps between ambient and 1233 K temperature range. The differential thermal analysis showed the ReS$_{2-x}$Se$_x$ (*x* = 0, 1, and 2) possesses initial endothermic followed by exothermic nature for fast heating rates. The kinetic parameters determined by the Kissinger relation show that all the single-crystal samples behavior is nearly the same when disintegrate at a higher-temperature range.

1 Introduction

Layered transition metal dichalcogenides called TMDC structure show immersive importance in application to their unique optical-electronic properties [1–7]. Apart from these, TMDCs having certain properties like high charge mobility, good stability, layered structure, and high surface area with excellent light absorption makes them prominent for photocatalysis, photodetector, solar cell, biological engineering, renewable energy, electrocatalyst kinds of applications [5–16]. Over the time, the researcher highly focused on molybdenum chalcogenides (MoS$_2$ and MoSe$_2$) and tin chalcogenides (SnS$_2$ and SnSe$_2$)

Address correspondence to E-mail: atriyghetiya@gmail.com; sunilchaki@yahoo.co.in

ⓢ Springer

for various kinds of applications [17–19]. Such TMDCs show layered dependent anisotropy in bandgap structure. Their bandgap converts indirect to direct while transforming from bulk layer to monolayer structure. In recent time, rhenium chalcogenides had attracted attention in various fields of applications. The new trending elements, rhenium chalcogenides $ReS_{2-x}Se_x$ ($x = 0$, 1, and 2), e.g., ReS_2, ReSSe, and $ReSe_2$, show distinctive properties in the era of optical- and electronic-based applications [3, 5, 8, 11–23]. Rhenium chalcogenides $ReS_{2-x}Se_x$ ($x = 0$, 1, and 2) have "Re$_4$" diamond-like coplanar chain structure. Rhenium chalcogenides single crystals show 1-T triclinic unit cell structure possessing weak layer-dependent properties [19, 24–26]. Transforming from bulk to monolayers, its direct bandgap properties remain same [21, 27]. The isotropy in optical property makes rhenium chalcogenides a good candidate in the optoelectronic study. The direct bandgap value for all possible dimensions (e.g., nanomaterial, thin films, layered as well as bulk crystals) shows its potential for application in all dimensional forms [22, 23, 28]. The electronics transport properties are also useful in energy conversion and storage-based applications.

In this work, single crystals of rhenium chalcogenides $ReS_{2-x}Se_x$ ($x = 0$, 1, and 2) are grown by chemical vapor transport (CVT) technique. Generally, the rhenium dichalcogenides material requires very high synthesis temperature values as per reports [19]. Here, the authors tried to minimize these high-temperature requirements and had grown fine rhenium dichalcogenides single crystals at low temperature. The various characterizations like UV–Vis–NIR spectroscopy (Kubelka–Munk plot), Raman spectroscopy, and thermal analysis are carried out and a comparative study within the series $ReS_{2-x}Se_x$ ($x = 0$, 1, and 2) is done. These studies will help in giving new era for optoelectronics device fabrications. Thermal analysis is further elaborated by calculating various thermal parameters. The thermodynamically stable 1-T Triclinic phase of rhenium chalcogenides has potential to be a good candidate for effective electrocatalysis and that leads to green renewable energy by following hydrogen evolution reaction (HER) and nitrogen reduction reaction (NRR) kind of reactions.

2 Experimental

The chemical vapor transport technique (CVT) is used with iodine as transporting agent in $ReS_{2-x}Se_x$ ($x = 0$, 1, and 2) single-crystals growth mechanism. The required metallic powders used for growing crystals are rhenium metal powder (SRL, India, 99.9999% pure), sulfur powder (Alfa Aesar USA, 99.99% pure), and selenium powder (Alfa Aesar USA, 99.99% pure). The quartz ampoules are employed to grow the single crystals. The ampoules are washed with hydrochloric (HCl) and sulfuric (H_2SO_4) acids, as they work as oxidizing agents to make inner surface cleaner, followed by hydrofluoric (HF) acid wash to roughen the inner surface giving sites to start nucleation for crystal growth. The final wash is given by rinsing with double distilled water. The elemental compositions as per required amount along with transport agent are loaded in a dried ampoule. The total weight of the stoichiometric elemental composition loaded into the quartz ampoule is approximately 8 g. The transporting agent iodine amount is taken at the rate of 4 mg/cm^3 of ampoule dimension. The dimension of the used quartz ampoule is 2 cm (inner diameter) and 20 cm (length). The quartz ampoule with elemental constituents is sealed after evacuation to 10^{-5} Torr. The vacuum-sealed ampoule containing the constituent elements is well shaken to mix metallic powder before inserting into the furnace. The complete elemental mixture is kept at one end of the ampoule tube called as source zone and the empty end is called as growth zone. The vacuum-sealed ampoule is inserted in a horizontal tubular furnace. The detailed growth mechanism for ReS_2 single crystal is mentioned in a previously published article of the authors [29]. In the growth of $ReS_{2-x}Se_x$ ($x = 0$, 1, and 2) single crystal, the temperature rising rate of the furnace is kept at 15 K/h such that the elemental mix-loaded quartz ampoule source zone is at 1075 K and growth zone is at 1025 K. Next the ampoule temperature is further raised to single-crystal growth temperatures such that source zone is kept at 1372 K and growth zone is kept at 1322 K. The low heating rate is taken to avoid damage to the quartz ampoule due to instant increase of vapor pressure. The ampoule is kept in this growth temperature gradient for 120 h. Maintaining temperature gradient for a finite time period leads to transport of metallic vapor. On completion of the growth run, the furnace temperature is slowly cooled

down to ambient conditions at a slow cooling rate of 30 K/h. Slow cooling is preferred to avoid thermal cracks in the grown single crystals. After removing it from the furnace, the as-grown single crystals are achieved. The schematic diagram of CVT techniques along with reaction formulas is shown in Fig. 1. The photograph of average large size CVT as-grown $ReS_{2-x}Se_x$ ($x = 0$, 1, and 2) single crystals are shown in Fig. 2. The photographs are captured by Nikon Coolpix L21 8.0 MP camera. The grown single crystals are shining brownish black in color with average large size dimensions of 5 mm $\times$ 5 mm $\times$ 2 mm.

3   Characterization
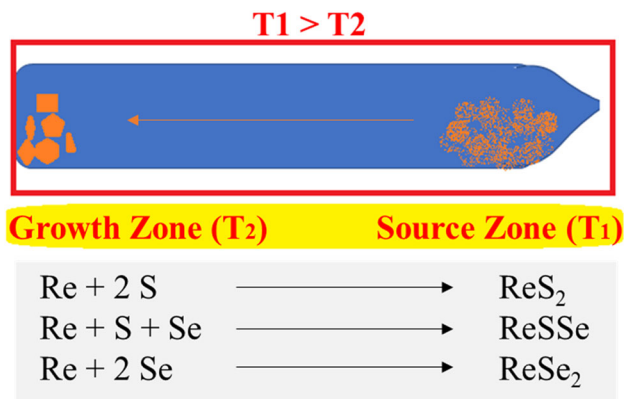
The CVT as-grown $ReS_{2-x}Se_x$ ($x = 0$, 1, and 2) single crystals are characterized for quantitative and qualitative analysis before performing in-depth thermal analysis. The X-ray diffraction (XRD) patterns of the single-crystal samples are recorded using Philips X′PERT MPD powder X-ray diffractometer. The Cu target X-ray tube is used to record the XRD by maintaining power of 2 kW with accuracy of $\pm$ 0.0025 in the 2θ range of 10° to 80°. The unit cell structure and the phase of the crystals are determined from the XRD using Powder X software. The stoichiometry of the single-crystal sample is determined by energy-dispersive analysis of X-rays (EDAX) technique attached to NOVA-450 electron microscope with integrated xT microscope control. The UV–Vis–NIR spectroscopy is done for the crystals using Shimadzu UV 3600 UV–Vis–NIR spectrometer. The Raman spectroscopy on the as-grown single crystals is done by the micro-Raman model STR 500 using

radiation source of 532 nm. The thermo-curves of the single-crystal samples are recorded using Seiko SII-EXSTAR TG/DTA-7200 thermal analyzer. The thermo-curves are measured in inert nitrogen atmosphere with a flow rate of 100 ml/s. The measurements are done for three different heating rates, 10 K/min, 15 K/min, and 20 K/min. The thermo-curves are recorded in temperature range of ambient and 1233 K.

4   Results and discussion

4.1   XRD

The XRD patterns of the as-grown $ReS_{2-x}Se_x$ ($x = 0$, 1 and 2) single crystals are shown in Fig. 3. The dominated plane orientation in the form of major peak (001) is same for all the $ReS_{2-x}Se_x$ ($x = 0$, 1, and 2) single crystals. The crystal structure determined from the XRD showed that all the crystals possess triclinic unit cell. The minute examination of the peaks position showed them to shift to lower 2θ values with increase in Se content. The shift occurs due to Vegard's law stating insertion of additional element lead to peak shift [30]. The lattice parameters of the ReS_2 are $a = 0.641$ nm, $b = 0.634$ nm, $c = 0.645$ nm, $\alpha = 91.60°$, $\beta = 105.04°$, and $\gamma = 118.97°$; ReSSe are $a = 0.658$, $b = 0.6572$ nm, $c = 0.6576$ nm, $\alpha = 91.51°$, $\beta = 104.79°$, and $\gamma = 119.07°$; and $ReSe_2$ are $a = 0.6602$ nm, $b = 0.6716$ nm, $c = 0.6728$ nm, $\alpha = 91.82°$, $\beta = 104.9°$, and $\gamma = 118.94°$ [21]. The assignment of Miller indices and lattice parameters is confirmed by Powder X software. The ReS_2 matches

Fig. 1 The schematic diagram for experimental technique of crystals growth
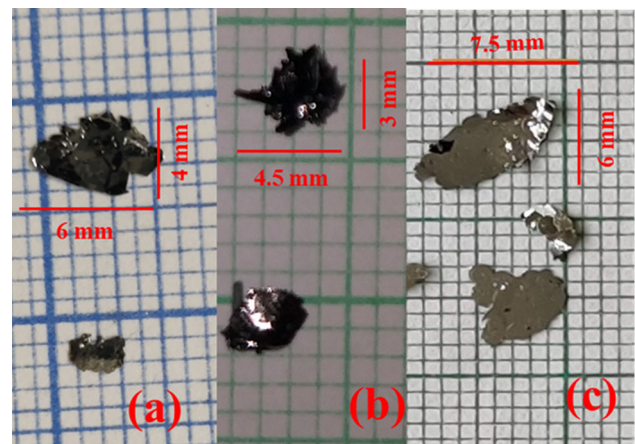
Fig. 2 The photographs of $ReS_{2-x}Se_x$ single crystals for **a** $x = 0$, **b** $x = 1$, and **c** $x = 2$
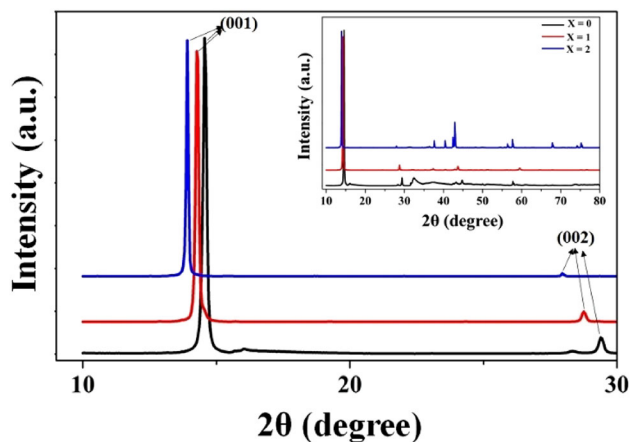
Fig. 3 The XRD of as-grown $ReS_{2-x}Se_x$ (x = 0, 1, and 2) single crystals

with standard JCPDS File No. 052-0818, similarly $ReSe_2$ with JCPDS File No. 04-007-1113 (Table 1).

4.2 EDAX

The recorded EDAX spectra of $ReS_{2-x}Se_x$ (x = 0, 1, and 2) are shown in Fig. 4. The absence of any unknown elemental peaks in spectra shows that the grown single crystals are contamination free. The observed atomic and weight percentages along with theoretical values are tabulated in Tables 2, 3, and 4. The tabulated data show that the respective single crystals are perfect stoichiometric.

4.3 Optical properties

The observed UV–Vis–NIR spectra for $ReS_{2-x}Se_x$ (x = 0, 1, and 2) single crystals are shown in Fig. 5. The spectra are recorded in reflectance mode in the wavelength range of 400–1200 nm. The reflectance edge lies in the range of 800–1000 nm. The band gap analysis is done using the Kubelka–Munk function, $[F(R)hv]^2 = A[hv - E_g]$ [31]. The direct bandgap values determined came out to be 1.37 eV of ReS_2, 1.31 eV of ReSSe, and 1.27 eV for $ReSe_2$ [28, 32, 33]. The analysis of the determined direct bandgap values states with increase of sulfur content the bandgap increases and as selenium content increases the bandgap decreases. The direct bandgap value is intermittent for equal sulfur and selenium contents. The variation of direct bandgap values with composition provides an opportunity to tailor the $ReS_{2-x}Se_x$ (x variable) composition according to the bandgap

Table 1 The lattice parameters of as-grown $ReS_{2-x}Se_x$ (x = 0, 1, and 2) single crystals

Lattice parameters	x = 0	x = 1	x = 2
a (nm)	0.641	0.658	0.660
b (nm)	0.634	0.657	0.671
c (nm)	0.645	0.658	0.672
α (°)	91.60	91.51	91.82
β (°)	105.04	104.79	104.9
γ (°)	118.97	119.07	118.94
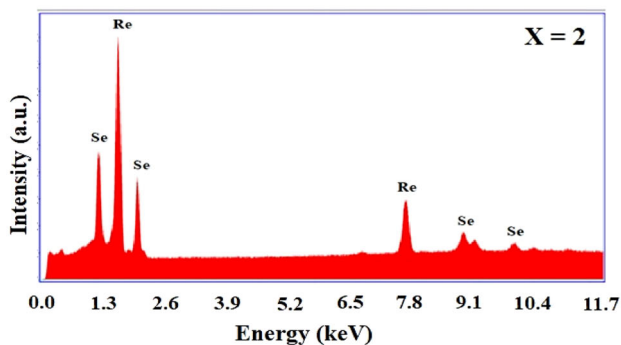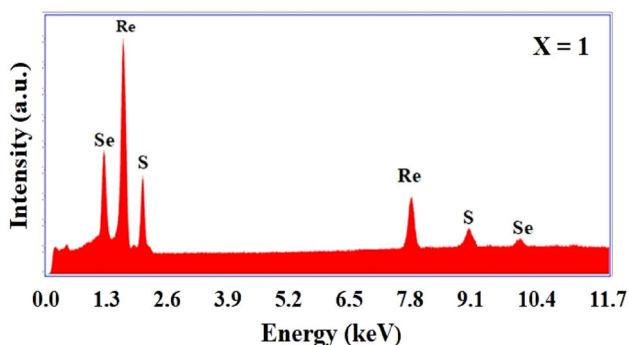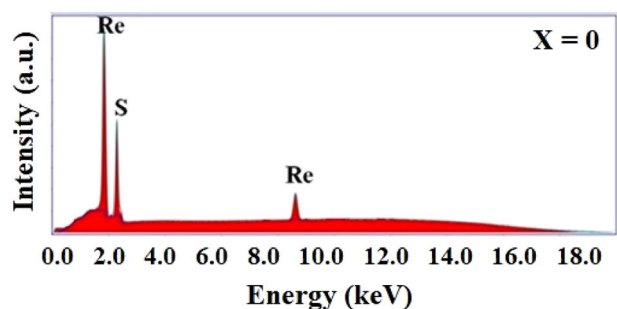
Fig. 4 The EDAX spectrum of as-grown ReS_2 single crystal. The EDAX spectrum of as-grown ReSSe single crystal. The EDAX spectrum of as-grown $ReSe_2$ single crystal

Table 2 The EDAX data of CVT as-grown ReS_2 single crystal

Element	Wt%		At.%	
	Observed	Theoretical	Observed	Theoretical
Re	74.27	74.38	65.84	66.66
S	25.73	25.62	34.16	33.33

Table 3 The EDAX data of CVT as-grown ReSSe single crystal

Element	Wt%		At.%	
	Observed	Theoretical	Observed	Theoretical
Re	63.97	62.65	34.23	33.33
S	10.28	10.79	32.70	33.33
Se	25.95	26.56	33.07	33.33

Table 4 The EDAX data of CVT as-grown $ReSe_2$ single crystal

Element	Wt%		At.%	
	Observed	Theoretical	Observed	Theoretical
Re	54.43	54.10	67.81	66.66
Se	45.57	45.90	32.19	33.33

requirement, thus providing a potential opportunity for application in optoelectronic devices.

4.4 Raman spectroscopy

The recorded Raman spectra of as-grown $ReS_{2-x}Se_x$ (x = 0, 1, and 2) single crystals are shown in Fig. 6. The atomic vibrational spectra of all the three single-crystal samples are recorded at 532-nm monochromatic wavelength at room temperature. The highly intense peaks for all three samples fall in the region of 100 cm^{-1} to 300 cm^{-1}. All observed peaks are well matched with the reported ones [3, 17, 29]. The similar patterns of all three crystals represent the same electronic configuration except valence cell. Two intense and characteristic vibration modes are observed at 150 cm^{-1} and 212 cm^{-1} for ReS_2, 141 cm^{-1} and 208 cm^{-1} for ReSSe, and 124 cm^{-1} and 158 cm^{-1} in the case $ReSe_2$.
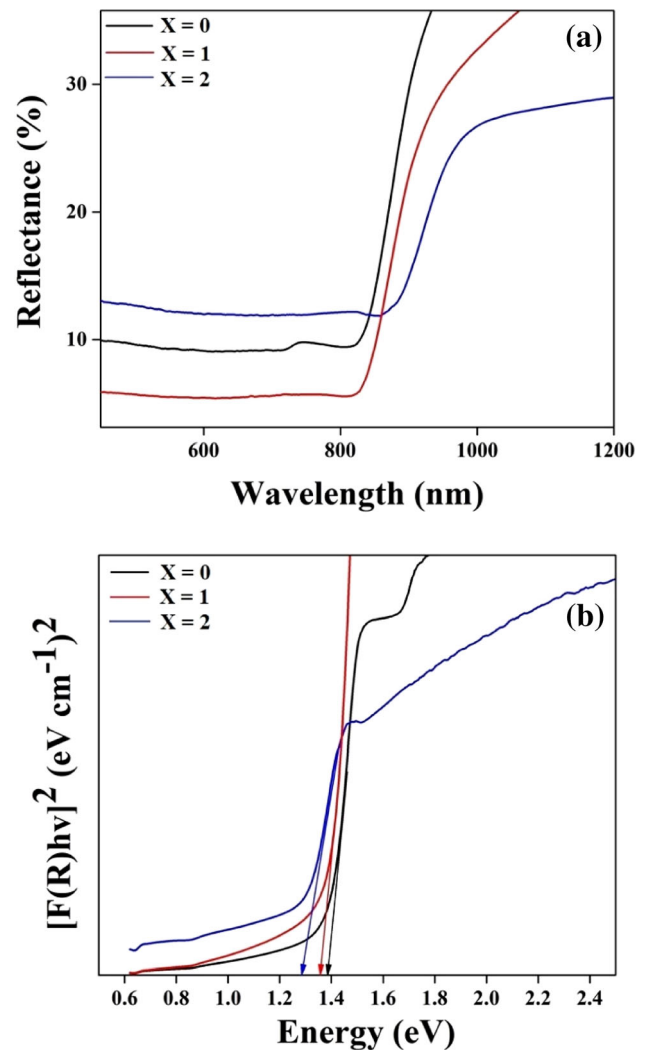

Fig. 5 **a** Reflectance and **b** Kubelka–Munk plots of $ReS_{2-x}Se_x$ (x = 0, 1, and 2) single crystals

4.5 Thermal analysis

The as-grown $ReS_{2-x}Se_x$ (x = 0, 1, and 2) single crystals are thermally analyzed up to temperature of 1233 K from the ambient conditions at three different heating rates, 10 K/min, 15 K/min, and 20 K/min. The analysis represents three different kinds of characterization, like thermal gravimetry (TG), differential thermal gravimetry (DTG), and differential thermal analysis (DTA). The thermo-curves of all three samples are shown below in Figs. 7, 8, and 9.

The thermal data show the weight loss increases with temperature for all heating rates. The curves show a minimal weight loss for Step I, ambient to 650 K, which is attributed to the evaporation of water and atmospheric surface-trapped molecules in the
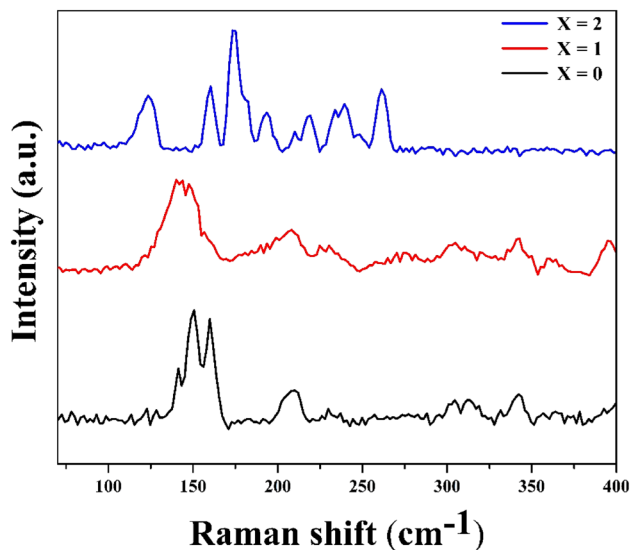
Fig. 6 The Raman spectra of CVT as-grown $ReS_{2-x}Se_x$ ($x = 0, 1,$ and 2) single crystals

sample. In Step II in temperature range of 650–1233 K shows major weight loss for all heating rates. The DTG peaks positions are also tabulated in the above tables for different heating rates.

The TG curves, Figs. 7a, 8a, and 9a show that the weight loss is different at different heating rates. This is due to the heat transfer restriction at a higher heating rate. The Step I analytically represents the minimal weight loss, below 1% in ambient to nearly 650 K temperature for all three heating rates, which arises due to the loss of moisture and atmospheric surface-trapped molecules from the samples. Also the excess of loosely attached elemental molecules gets removed in the Step I. These minor weight losses have perfect relation with heating rate, due to surface trapping nature. The major weight loss occurring in Step II shows the decomposition of the crystal samples. As tabulated in Tables 5, 6, and 7, the weight loss magnitude lies in the range of 20% to 80%, arising due to the decomposition of rhenium chalcogenides at higher-temperature range. The observation confirms that as the heating rate increases the weight loss increases, which occur due to unequal heat transition and non-equilibrium with surrounding molecules. Hence, the as-grown $ReS_{2-x}Se_x$ ($x = 0, 1,$ and 2) single crystals are found to be stable up to 650 K.
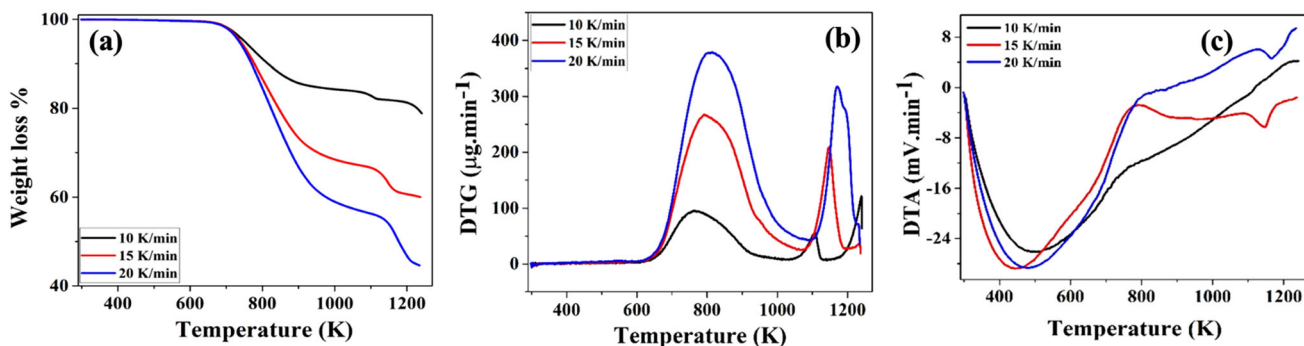
Fig. 7 **a** TGA, **b** DTG, and **c** DTA of CVT as-grown ReS_2 single crystals
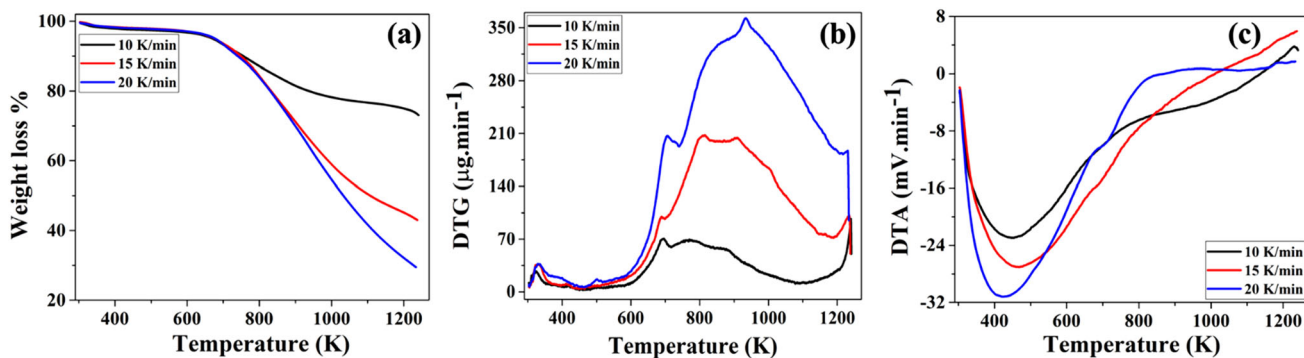
Fig. 8 **a** TGA, **b** DTG, and **c** DTA of CVT as-grown ReSSe single crystals
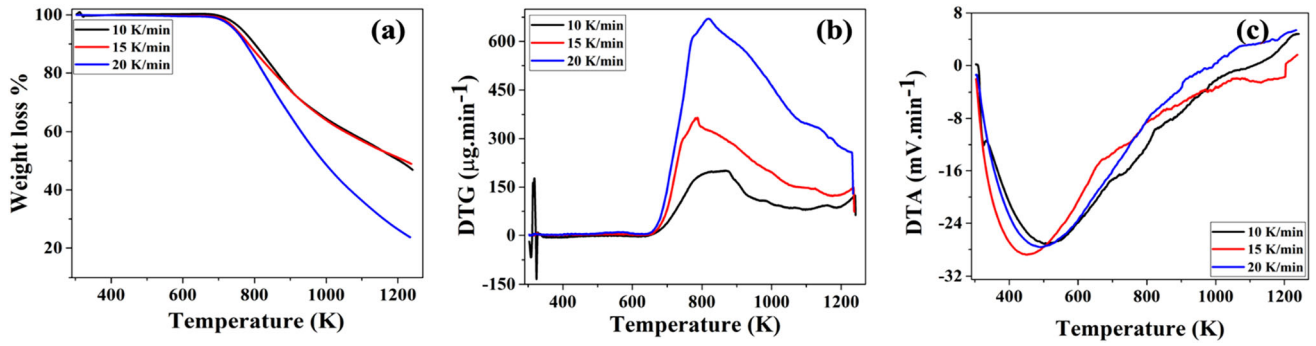
Fig. 9 **a** TGA, **b** DTG, and **c** DTA of CVT as-grown $ReSe_2$ single crystals

Table 5 Thermal data of CVT as-grown ReS_2 single crystal

Heating rates (K/min)	Weight loss (%)		Total weight loss (%)	DTG peak position, T_m (K)
	Temperature range (K)			
	Step I 300–650 K	Step II 650–1233 K	300–1233 K	2nd peak
10	0.57	19.67	20.24	764.99
15	0.65	39.30	39.95	791.96
20	0.84	54.35	55.19	812.43

Table 6 Thermal data of CVT as-grown ReSSe single crystal

Heating rates (K/min)	Weight loss (%)		Total weight loss (%)	DTG peak position, T_m (K)
	Temperature range (K)			
	Step I 300–650 K	Step II 650–1233 K	300–1233 K	2nd peak
10	4.48	21.93	26.41	864.12
15	4.18	30.84	35.02	899.63
20	3.88	66.43	70.31	919.29

Table 7 Thermal data of CVT as-grown $ReSe_2$ single crystal

Heating rates (K/min)	Weight loss (%)		Total weight loss (%)	DTG peak position, T_m (K)
	Temperature range (K)			
	Step I 300–650 K	Step II 650–1233 K	300–1233 K	2nd peak
10	0.04	52.40	52.44	784.23
15	0.11	50.48	50.59	789.12
20	0.71	75.42	76.13	818.20

The DTG curves shown in Figs. 7b, 8b, and 9b show the presence of peaks due to Step I and Step II. It confirms the two-step decomposition of the $ReS_{2-x}Se_x$ ($x = 0$, 1, and 2) single crystals. The DTA plots in Figs. 7b, 8b, and 9b show the endothermic nature followed by the exothermic nature. The initial endothermic nature is due to the vaporization of the moisture and excess loosely attached material from the given samples. The following exothermic nature corresponds to the decomposition of materials.

4.5.1 Kissinger relation

All the important thermal parameters for all three $ReS_{2-x}Se_x$ ($x = 0$, 1, and 2) single crystals are calculated by Kissinger relation using Eqs. (1) to (5) [34]. The relations of Kissinger are given below:

$$\ln\frac{\beta}{T_m^2} = \ln\frac{AR}{E_a} + \ln\left[\frac{d\{f(\alpha)\}}{d\alpha}\right] - \frac{E_a}{RT_m}, \quad (1)$$

where 'α' is the fraction of weight loss and $f(\alpha)$ is the function which relies on the value of α. This equation is strictly constrained to first-order reaction value as per the kinetic model, i.e., $d[f(\alpha)]/d\alpha = -1$. Therefore, the $d[f(\alpha)]/d\alpha$ term is eliminated and further it turns more significant.

$$\ln\frac{\beta}{T_m^2} = \ln\frac{AR}{E_a} - \frac{E_a}{RT_m}. \quad (2)$$

Here, β is the heating rate, T_m is the DTG peak position, and R is the gas constant. The Kissinger plots between $\ln\frac{\beta}{T_m^2}$ and $\frac{1}{T_m}$ for CVT as-grown $ReS_{2-x}Se_x$ ($x = 0$, 1, and 2) single crystals are shown in Fig. 10.

The parameters are calculated for further detailed analysis using following equations [34]:

$$\Delta H = E_a - RT_m, \quad (3)$$

$$\Delta S = 2.303\ R\log\left(\frac{Ah}{kT_m}\right), \quad (4)$$

$$\Delta G = \Delta H - T\Delta S. \quad (5)$$

The parameters calculated for Step II are tabulated in Table 8.

The determined ΔS values, Table 8, show that it is negative for all $ReS_{2-x}Se_x$ ($x = 0$, 1, and 2) crystals. The negative ΔS value states ordering happen with the rise in temperature and the crystals get ordered before structure degradation. The determined
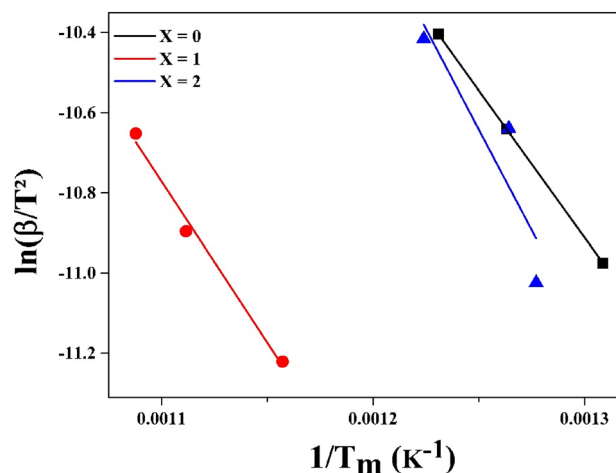
Fig. 10 The Kissinger plots for $ReS_{2-x}Se_x$ ($x = 0$, 1, and 2) CVT as-grown single crystals

ΔH values are positive for all the $ReS_{2-x}Se_x$ ($x = 0$, 1, and 2) single crystals that state the heat absorption is by the single crystals. The large heat absorption leads to disintegration of $ReS_{2-x}Se_x$ ($x = 0$, 1, and 2) single crystals. The disintegration is corroborated by the maximum weight loss in the temperature range of Step II. The ΔG values are positive in case of all the $ReS_{2-x}Se_x$ ($x = 0$, 1, and 2) single crystals. The positive ΔG values state that the process of disintegration to be non-spontaneous. All the parameters calculated are for Step II. The overall graphical picture is mainly highlighted for Step II disintegration due to high heat absorption than Step I.

5 Conclusion

The single crystals of $ReS_{2-x}Se_x$ ($x = 0$, 1, and 2) are successfully grown by chemical vapor transport technique using iodine as transporting agent. The temperature range employed in the present growth technique is too lower compared to the melting points of rhenium chalcogenide. This is possible due to chemical vapor transport reaction. The powder XRD of as-grown crystals showed them to be of single phase. $ReS_{2-x}Se_x$ ($x = 0$, 1, and 2) have triclinic unit cell structure in good match with the reported data. The crystal orientation is along major (001) plane. The EDAX of the crystals showed them to be free of any impurity and overall stoichiometry is well maintained in all as-grown single crystals. The optical analysis shows that the bandgap values vary with sulfur–selenium composition. The direct optical

Table 8 The kinetic parameters of $ReS_{2-x}Se_x$ ($x = 0$, 1, and 2) single crystals

Single crystals	E_a (J/mole)	ΔS (J/K mole)	ΔH (J/mole)	ΔG (J/mole)
ReS_2	61,453.70	$-$ 189.75	54,894.01	204,614.42
ReSSe	67,337.58	$-$ 194.67	59,904.86	233,947.28
$ReSe_2$	80,019.46	$-$ 201.89	73,380.32	258,123.87

bandgap lies between 1.37 and 1.27 eV for different compositions. The variation in energy gap is due to the changes in energy level of the host material. The Raman spectroscopy of the crystals showed all the peaks of $ReS_{2-x}Se_x$ ($x = 0$, 1, and 2). The TG analysis showed the CVT as-grown $ReS_{2-x}Se_x$ ($x = 0$, 1, and 2) single-crystal samples to disintegrate in two steps: the first Step I represents the good thermal stability of grown materials and the second Step II is disintegration which is further deeply analyzed with the required calculation and parameters. The two-step disintegration is supported by the presence of two peaks in the corresponding DTG curves. The corresponding DTA showed an initial endothermic and later exothermic nature. The thermodynamic parameters determined using Kissinger relations shows the thermal activation energy value is high in the high-temperature range for Step II. This indicates the decomposition of the sample at high temperatures. The changes in entropy of all samples are found negative. The change in enthalpy is positive which indicates heat absorption by the samples. The change in Gibbs free energy values are positive stating prompt non-spontaneous absorption of heat as temperature rises. The thermodynamic parameters showed that the single-crystal sample disintegrates at high temperatures leading to weight loss being observed in the TG curves.

Author contributions

All authors have contributed to conception and design. Material preparation, analysis, and drafting of the manuscript were performed by ABG. The resources, analysis, drafting of the manuscript, and approval have been done by SHC. The drafting, data collection, and former analysis have been done by JPT. The resources and drafting have been done by MPD.

Declarations

Conflict of interest The authors declare that they have no known financial interest or personal relationship that could have appeared to influence the work reported in this paper. All the authors declare that there are no competing interests involved in the research work reported in the manuscript submitted for publication to this esteemed journal.

References

1. V. Urbanová, N. Antonatos, J. Plutnar, P. Lazar, J. Michalička, M. Otyepka, Z. Sofer, M. Pumera, ACS Nano **15**, 2374 (2021)
2. K. Kalantar-Zadeh, J.Z. Ou, T. Daeneke, M.S. Strano, M. Pumera, S.L. Gras, Adv. Funct. Mater. **25**, 5086 (2015)
3. F. Liu, S. Zheng, A. Chaturvedi, V. Zólyomi, J. Zhou, Q. Fu, C. Zhu, P. Yu, Q. Zeng, N.D. Drummond, H.J. Fan, C. Kloc, V.I. Fal'ko, X. He, Z. Liu, Nanoscale **8**, 5826 (2016)
4. M.Z. Iqbal, S. Alam, M.M. Faisal, S. Khan, Int. J. Energy Res. **43**, 3058 (2019)
5. S. Han, S. Zhou, X. Liu, Y. Liu, S. Zhang, X. Yang, Laser Phys. Lett. **15**, 08504 (2018)
6. X. Zhang, S.Y. Teng, A.C.M. Loy, B.S. How, W.D. Leong, X. Tao, Nanomaterials **10**(6), 1012 (2020)
7. S. Li, B. Li, X. Feng, L. Chen, Y. Li, L. Huang, X. Fong, K.W. Ang, NPJ 2D Mater. Appl. **5**, 1 (2021)
8. S.R. Yousefi, H.A. Alshamsi, O. Amiri, M. Salavati-Niasari, J. Mol. Liq. **337**, 116405 (2021)

9. M.A. Mahdi, S.R. Yousefi, L.S. Jasim, M. Salavati-Niasari, Int. J. Hydrog. Energy 47, 14319 (2022)

10. S.R. Yousefi, A. Sobhani, H.A. Alshamsi, M. Salavati-Niasari, RSC Adv. 11, 11500 (2021)

11. S.R. Yousefi, M. Masjedi-Arani, M.S. Morassaei, M. Salavati-Niasari, H. Moayedi, Int. J. Hydrog. Energy 44, 24005 (2019)

12. S.R. Yousefi, A. Sobhani, M. Salavati-Niasari, Adv. Powder Technol. 28, 1258 (2017)

13. S.R. Yousefi, O. Amiri, M. Salavati-Niasari, Ultrason. Sonochem. 58, 104619 (2019)

14. S.R. Yousefi, M. Ghanbari, O. Amiri, Z. Marzhoseyni, P. Mehdizadeh, M. Hajizadeh-Oghaz, M. Salavati-Niasari, J. Am. Ceram. Soc. 104, 2952 (2021)

15. S.R. Yousefi, D. Ghanbari, M. Salavati-Niasari, M. Hassanpour, J. Mater. Sci. Mater. Electron. 27, 1244 (2016)

16. S.R. Yousefi, D. Ghanbari, M. Salavati-Niasari, J. Nanostruct. 6, 80 (2016)

17. C. Li, Y. Leng, J. Huo, Appl. Sci. 8(10), 1753 (2018)

18. J. Luxa, P. Marvan, P. Lazar, Z. Sofer, Nanoscale 11, 14684 (2019)

19. B. Jariwala, D. Voiry, A. Jindal, B.A. Chalke, R. Bapat, A. Thamizhavel, M. Chhowalla, M. Deshmukh, A. Bhattacharya, Chem. Mater. 28, 3352 (2016)

20. Y. Von Lim, S. Huang, Q. Wu, Y. Zhang, D. Kong, Y. Wang, T. Xu, Y. Shi, Q. Ge, L.K. Ang, H.Y. Yang, Nano Energy 61, 626 (2019)

21. J.Q. Zong, S.F. Zhang, W.X. Ji, C.W. Zhang, P. Li, P.J. Wang, J. Nanomater. 2019, 1–8 (2019)

22. A. Zulkefli, B. Mukherjee, T. Iwasaki, R. Hayakawa, S. Nakaharai, Y. Wakayama, Jpn. J. Appl. Phys. 60(58), SBBH01 (2021)

23. Y. Cui, F. Lu, X. Liu, Sci. Rep. 7, 1 (2017)

24. P. Schiettecatte, A. Rousaki, P. Vandenabeele, P. Geiregat, Z. Hens, Langmuir 36, 15493 (2020)

25. C.H. Ho, Y.S. Huang, P.C. Liao, K.K. Tiong, J. Phys. Chem. Solids 60, 1797 (1999)

26. H.J. Lamfers, A. Meetsma, G.A. Wiegers, J.L. De Boer, J. Alloys Compd. 241, 34 (1996)

27. S. Sim, D. Lee, J. Lee, M. Cha, S. Cha, W. Heo, S. Cho, W. Shim, K. Lee, J. Yoo, R.P. Prasankumar, H. Choi, M.H. Jo, Phys. Rev. B 101, 1 (2020)

28. D.A. Chenet, O.B. Aslan, P.Y. Huang, C. Fan, A.M. Van Der Zande, T.F. Heinz, J.C. Hone, Nano Lett. 15, 5667 (2015)

29. A. Ghetiya, S.H. Chaki, A.J. Khimani, A.B. Hirpara, R.M. Kannaujiya, S. Patel, M.P. Deshpande, Phys. Status Solidi Appl. Mater. Sci. 218, 1 (2021)

30. C.P. Kempter, Phys. Status Solidi 18, K117 (1966)

31. S.S. Abdullahi, S. Güner, Y. Koseoglu, I.M. Musa, B.I. Adamu, M.I. Abdulhamid, J. Niger. Assoc. Math. Phys. 35, 241 (2016)

32. D. Ghoshal, A. Yoshimura, T. Gupta, A. House, S. Basu, Y. Chen, T. Wang, Y. Yang, W. Shou, J.A. Hachtel, J.C. Idrobo, T.M. Lu, S. Basuray, V. Meunier, S.F. Shi, N. Koratkar, Adv. Funct. Mater. 28, 1 (2018)

33. R. Wang, J. Han, P. Xu, T. Gao, J. Zhong, X. Wang, X. Zhang, Z. Li, L. Xu, B. Song, Adv. Sci. 7 (2020)

34. R. Plumadore, M.M. Al Ezzi, S. Adam, A. Luican-Mayer, J. Appl. Phys. 128(4), 044303 (2020)